



An extended residual-based variational multiscale method for two-phase flow including surface tension

U. Rasthofer^{a,b}, F. Henke^{a,b}, W.A. Wall^b, V. Gravemeier^{a,b,*}

^a Emmy Noether Research Group "Computational Multiscale Methods for Turbulent Combustion", Technische Universität München, Boltzmannstr. 15, 85748 Garching, Germany

^b Institute for Computational Mechanics, Technische Universität München, Boltzmannstr. 15, 85748 Garching, Germany

ARTICLE INFO

Article history:

Received 4 August 2010

Received in revised form 12 January 2011

Accepted 4 February 2011

Available online 21 March 2011

Keywords:

Two-phase flow

Variational multiscale method

Extended finite element method

Level-set method

ABSTRACT

In this study, an extended residual-based variational multiscale method is proposed for two-phase flow including surface tension. The extended residual-based variational multiscale method combines a residual-based form of the variational multiscale method and the extended finite element method (XFEM). By extending the solution spaces, it is possible to reproduce discontinuities of the solution fields inside elements intersected by the interface. In particular, we propose a quasi-static enrichment to reproduce time-dependent discontinuities. Kink enrichments of both velocity and pressure as well as kink enrichments of velocity combined with jump enrichments of pressure are considered here. To capture the interface between the phases on a fixed grid, a level-set approach is used. A residual-based variational multiscale method is employed for computing both flow and interface motion. The presented method is tested for various two-phase flow examples exhibiting small and large density and viscosity ratios, with and without surface tension: a two-phase Couette flow, a Rayleigh–Taylor instability, a sloshing tank and a three-dimensional rising bubble. To the best of our knowledge, these are the first simulation results for representative time-dependent three-dimensional two-phase flow problems using an extended finite element method. Stable and accurate results are obtained for all test examples.

© 2011 Elsevier B.V. All rights reserved.

1. Introduction

As two-phase flows are widely encountered in engineering and environmental applications, the development of simulation approaches for such problems has gained great attention. Compared to single-phase flow problems, an additional challenge is posed by the correct handling of the interface between the phases as well as the behavior of the phases at the interface. In two-phase flows, velocity and pressure field exhibit discontinuities across the interface which have to be taken into account.

For resolving the interface between the two phases, two types of methods are generally distinguished: interface-tracking and interface-capturing methods. In interface-tracking methods, the mesh explicitly represents the interface and follows its movement throughout the simulation. In contrast, in interface-capturing methods, the interface is described implicitly by an auxiliary function, which is defined on the fixed mesh. A convenient interface-

capturing approach is the level-set method (see, e.g., [1,2]), which was described for two-phase flows, for example, in [3]. Applications to two-phase flow problems using (stabilized) finite element methods along with level-set approaches can be found, e.g., in [4,5].

However, if elements are intersected by the interface when using a level-set method, a standard finite element method (FEM) is not able to adequately reproduce the discontinuous gradient of the velocity field and the discontinuity of the pressure field inside intersected elements. To take into account these discontinuities, the extended (or enriched) finite element method (XFEM) is used in this study. The XFEM was originally developed for crack problems (see, e.g., [6]), but has been applied to many other problem configurations by now, among them also two-phase flows, e.g., in [7,8]. In the XFEM, the approximation space is extended in such a way that known properties of the solution field such as kinks or jumps can be represented.

In this work, a residual-based variational multiscale FEM as originally proposed in a general form, e.g., in [9] is employed for computing flow as well as interface motion. For the flow problem, in particular, we use a form of the residual-based variational multiscale method containing streamline/upwind Petrov–Galerkin (SUPG) term, pressure stabilizing Petrov–Galerkin (PSPG) term and grad–div (or bulk-viscosity) term as proposed for the generalized Oseen problem in [10]. The application of the residual-based

* Corresponding author at: Emmy Noether Research Group "Computational Multiscale Methods for Turbulent Combustion", Technische Universität München, Boltzmannstr. 15, 85748 Garching, Germany. Tel.: +49 (0) 89 28915245; fax: +49 (0) 89 28915301.

E-mail addresses: rasthofer@inm.mw.tum.de (U. Rasthofer), henke@inm.mw.tum.de (F. Henke), wall@inm.mw.tum.de (W.A. Wall), vgravem@inm.mw.tum.de (V. Gravemeier).

variational multiscale method to the level-set equation yields an SUPG term in the corresponding variational formulation. Additional cross- and Reynolds-stress terms as proposed particularly for turbulent incompressible flow problems in [11] are not considered here, since all flow examples in this study remain within a laminar flow regime.

Some differences of the present work compared to XFEMs proposed earlier and methods similar to XFEM for two-phase flows are pointed out in the following. In [7], an XFEM taking into account gradient discontinuities of the velocity field was proposed. Therein, the convective terms were stabilized by a characteristic based split (CBS) method as proposed in, e.g., [12]. Studies using XFEMs, but restricted to problems governed by the Stokes equations, were presented in [8,13]. Instead of using additional stabilization terms, inf-sup-stable elements were employed in those studies. Jumps in the pressure field due to surface-tension effects were examined in [8], and the proposed method was tested for a three-dimensional stationary bubble. In [13], the XFEM in conjunction with the level-set method was further extended for n-phase flows involving more than two fluids. Therein, an enrichment function accounting for various interfaces within one element was derived. An alternative XFEM for two-phase flows, named intrinsic XFEM, was recently proposed in [14]. Within the intrinsic XFEM, instead of introducing additional degrees of freedom, inner-element discontinuities were reproduced by the use of intrinsically enriched shape functions developed via a moving least-squares method. Moreover, a stabilized FEM, including SUPG and PSPG terms, but no grad-div term, was employed for solving the fluid field. An SUPG term was also added to the variational formulation of the level-set field.

Methods similar to the XFEM were developed for two-phase flows, e.g., in [15,16]. A method taking into account discontinuities of the pressure field and gradient discontinuities of the velocity field was described in [15]. In that study, inf-sup-stable elements were employed. While the pressure field was enriched similar to an XFEM, the enrichment of the velocity field was constructed based on bubble functions. To demonstrate the presented method, a three-dimensional particle with high surface tension, rising towards a fluid–fluid interface, was shown. In [16], an alternative approach for gradient discontinuities of the pressure was developed. An additional degree of freedom, local to intersected elements, was introduced and could therefore be condensed. A stabilized FEM of algebraic-subgrid-scale (ASGS) type was used for the fluid field.

In comparison to the aforementioned studies, we propose an XFEM similar to the approaches presented in [7,8,13], however, applied in combination with a residual-based variational multiscale method containing SUPG/PSPG/grad-div terms. This stabilization approach is similar to the one used in [16]. In addition, a quasi-static enrichment strategy is introduced, which turned out to be more stable when capturing moving discontinuities. The method is tested for various numerical examples with and without surface tension, including a challenging three-dimensional rising bubble.

The present study is organized as follows. In Section 2, the governing equations are described. Afterwards, a residual-based variational multiscale formulation is derived in Section 3. The XFEM approximation for the velocity and the pressure field is presented in Section 4. The introduced method is then tested for various two- and three-dimensional two-phase flow problems in Section 5. Conclusions from this study are drawn in Section 6.

2. Statement of the problem

2.1. Fluid field

A domain Ω , which is partitioned into two subdomains, Ω^+ and Ω^- with $\Omega = \Omega^+ \cup \Omega^-$ and $\Omega^+ \cap \Omega^- = \emptyset$, is considered, see Fig. 1.

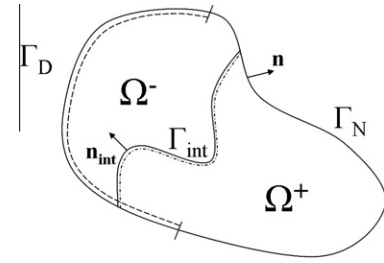


Fig. 1. Subdomains separated by an interface.

Each subdomain contains fluid, but the two fluids in Ω^+ and Ω^- have different constant densities ρ and viscosities μ :

$$\rho(\mathbf{x}, t) = \begin{cases} \rho^- & \forall \mathbf{x} \in \Omega^- \\ \rho^+ & \forall \mathbf{x} \in \Omega^+ \end{cases}, \quad \mu(\mathbf{x}, t) = \begin{cases} \mu^- & \forall \mathbf{x} \in \Omega^- \\ \mu^+ & \forall \mathbf{x} \in \Omega^+ \end{cases}.$$

Furthermore, the two fluids are assumed immiscible. The interface separating the phases is denoted by Γ_{int} , with the normal vector \mathbf{n}_{int} pointing into the domain Ω^- . The flows in both subdomains are mathematically described by the incompressible Navier–Stokes equations, which read in convective form as

$$\rho \frac{\partial \mathbf{u}}{\partial t} + \rho \mathbf{u} \cdot \nabla \mathbf{u} + \nabla p - \nabla \cdot (2\mu \varepsilon(\mathbf{u})) = \rho \mathbf{g}, \quad (1)$$

$$\nabla \cdot \mathbf{u} = 0, \quad (2)$$

where \mathbf{u} denotes the velocity, p the pressure, $\varepsilon(\mathbf{u}) = \frac{1}{2}(\nabla \mathbf{u} + (\nabla \mathbf{u})^T)$ the rate-of-deformation tensor and \mathbf{g} the gravity force vector. To close the problem, initial as well as Dirichlet and Neumann boundary conditions are prescribed

$$\mathbf{u}(\mathbf{x}, t = 0) = \mathbf{u}_0(\mathbf{x}) \quad \text{in } \Omega,$$

$$\mathbf{u} = \mathbf{u}_D \quad \text{on } \Gamma_D,$$

$$\boldsymbol{\sigma} \cdot \mathbf{n} = \mathbf{h} \quad \text{on } \Gamma_N,$$

where $\boldsymbol{\sigma} = -p\mathbf{I} + 2\mu \varepsilon(\mathbf{u})$ denotes the Cauchy stress tensor. It is assumed that $\Gamma_D \cap \Gamma_N = \emptyset$, $\Gamma_D \cup \Gamma_N = \Gamma$, and \mathbf{n} denotes the outer unit normal vector on the boundary Γ . If no-slip boundary conditions along the interface and zero mass transfer across the interface are assumed, a continuous velocity field at the interface is obtained:

$$[[\mathbf{u}]] = 0, \quad (3)$$

where $[[\cdot]]$ denotes the jump across Γ_{int} . Moreover, surface tension along the interface is balanced with a jump in the normal stress

$$[[\boldsymbol{\sigma} \cdot \mathbf{n}_{\text{int}}]] = \gamma \kappa \mathbf{n}_{\text{int}}, \quad (4)$$

where γ is the surface tension coefficient and κ the curvature of the interface Γ_{int} .

2.2. Level-set field

The level-set method is used to describe the motion of the interface. The location of the interface between the two phases is represented by an implicit function Φ , with the zero level-set $\Phi(\mathbf{x}, t) = 0$ representing the interface. It follows for two-phase flows that

$$\Phi(\mathbf{x}, t) \begin{cases} > 0 & \forall \mathbf{x} \in \Omega^+, \\ = 0 & \forall \mathbf{x} \in \Gamma_{\text{int}}, \\ < 0 & \forall \mathbf{x} \in \Omega^-. \end{cases}$$

The evolution of Φ is governed by the level-set equation

$$\frac{\partial \Phi}{\partial t} + \mathbf{u} \cdot \nabla \Phi = 0, \quad (5)$$

where \mathbf{u} denotes the velocity field obtained from solving the Navier–Stokes equations. Usually, Φ is initially defined as a signed distance function

$$\Phi(\mathbf{x}, t = 0) = d,$$

where d is the distance function which is positive/negative in Ω^+/Ω^- .

While Eq. (5) moves the zero level-set, Φ may deviate from a signed distance function. Without reinitializing Φ to a signed distance function periodically throughout the calculation, unphysical results may be observed. The reader is referred to, e.g., [17] and references therein for a detailed description of different reinitialization techniques. Here, the reinitialization is performed by directly calculating the distance of each grid point from the zero isocontour of the level-set.

3. Residual-based variational multiscale formulation

3.1. Fluid field

The goal of this section is to present a residual-based variational multiscale formulation for the fluid field. Assuming appropriate solution function spaces $\mathcal{S}_{\mathbf{u}}$ for \mathbf{u} and \mathcal{S}_p for p as well as weighting function spaces $\mathcal{V}_{\mathbf{u}}$ for \mathbf{v} and \mathcal{V}_p for q , a variational formulation for (1) and (2) is given as follows: find $p \in \mathcal{S}_p$ and $\mathbf{u} \in \mathcal{S}_{\mathbf{u}}$ such that

$$\left(\mathbf{v}, \rho \frac{\partial \mathbf{u}}{\partial t} \right) + (\mathbf{v}, \rho \mathbf{u} \cdot \nabla \mathbf{u}) - (\nabla \cdot \mathbf{v}, p) + (\varepsilon(\mathbf{v}), 2\mu \varepsilon(\mathbf{u})) = (\mathbf{v}, \rho \mathbf{g}) + (\mathbf{v}, \mathbf{h}_{\mathbf{u}})_{\Gamma_{\text{N}}} + (\mathbf{v}, \gamma \kappa \mathbf{n}_{\text{int}})_{\Gamma_{\text{int}}} \quad \forall \mathbf{v} \in \mathcal{V}_{\mathbf{u}}, \quad (6)$$

$$(q, \nabla \cdot \mathbf{u}) = 0 \quad \forall q \in \mathcal{V}_p, \quad (7)$$

where $(\cdot, \cdot) = (\cdot, \cdot)_{\Omega}$ and $(\cdot, \cdot)_{\Gamma_{\text{N}}/\Gamma_{\text{int}}}$ denote the usual L_2 -inner product on Ω and $\Gamma_{\text{N}}/\Gamma_{\text{int}}$, respectively. Compared to one-phase flows, the last term on the right hand side of (6) is the only additional term in the two-phase flow formulation. This term results from integration-by-parts and summing up the interface terms belonging to the subdomains Ω^+ and Ω^-

$$(\mathbf{v}, \boldsymbol{\sigma}^+ \cdot \mathbf{n}_{\text{int}}^+)_{\Gamma_{\text{int}}} + (\mathbf{v}, \boldsymbol{\sigma}^- \cdot \mathbf{n}_{\text{int}}^-)_{\Gamma_{\text{int}}} = (\mathbf{v}, \boldsymbol{\sigma}^+ \cdot \mathbf{n}_{\text{int}} - \boldsymbol{\sigma}^- \cdot \mathbf{n}_{\text{int}})_{\Gamma_{\text{int}}} = (\mathbf{v}, \gamma \kappa \mathbf{n}_{\text{int}})_{\Gamma_{\text{int}}},$$

with $\mathbf{n}_{\text{int}} = \mathbf{n}_{\text{int}}^+ = -\mathbf{n}_{\text{int}}^-$.

A variational projection for separating resolved and unresolved scales within an FEM is assumed. Hence, pressure and velocity fields are decomposed via variational projection into resolved and unresolved (or subgrid) parts as

$$p = p^h + \hat{p}, \quad (8)$$

$$\mathbf{u} = \mathbf{u}^h + \hat{\mathbf{u}}. \quad (9)$$

The subgrid-scale parts of pressure and velocity field are approximated in an elementwise manner based on the resolved-scale parts. Hence, in each element, the subgrid-scale parts are given as

$$\hat{p} = -\tau_c \mathcal{R}_c^h, \quad (10)$$

$$\hat{\mathbf{u}} = -\tau_M \mathcal{R}_M^h \quad (11)$$

using respective stabilization parameters τ , which will be defined below. The discrete residuals of mass conservation (or continuity equation) and momentum conservation read as

$$\mathcal{R}_c^h = \nabla \cdot \mathbf{u}^h, \quad \mathcal{R}_M^h = \rho \frac{\partial \mathbf{u}^h}{\partial t} + \rho \mathbf{u}^h \cdot \nabla \mathbf{u}^h + \nabla p^h - \nabla \cdot (2\mu \varepsilon(\mathbf{u}^h)) - \rho \mathbf{g}.$$

For a detailed description of residual-based multiscale approximations leading to stabilized methods, the reader is referred to, e.g., [9]. The residual-based variational multiscale finite element formulation is obtained by introducing decompositions (8) and (9) and approximations (10) and (11) into the variational formulation (6)

and (7), integrating by parts some terms and omitting other terms: find $p^h \in \mathcal{S}_p^h$ and $\mathbf{u}^h \in \mathcal{S}_{\mathbf{u}}^h$ such that

$$\begin{aligned} & \left(\mathbf{v}^h, \rho \frac{\partial \mathbf{u}^h}{\partial t} \right) + (\mathbf{v}^h, \rho \mathbf{u}^h \cdot \nabla \mathbf{u}^h) - (\nabla \cdot \mathbf{v}^h, p^h) + (\varepsilon(\mathbf{v}^h), 2\mu \varepsilon(\mathbf{u}^h)) \\ & + (\nabla \cdot \mathbf{v}^h, \tau_c \mathcal{R}_c^h) + (\rho \mathbf{u}^h \cdot \nabla \mathbf{v}^h, \tau_M \mathcal{R}_M^h) \\ & = (\mathbf{v}^h, \rho \mathbf{g}) + (\mathbf{v}^h, \mathbf{h}_{\mathbf{u}})_{\Gamma_{\text{N}}} + (\mathbf{v}^h, \gamma \kappa \mathbf{n}_{\text{int}})_{\Gamma_{\text{int}}} \quad \forall \mathbf{v}^h \in \mathcal{V}_{\mathbf{u}}^h, \end{aligned} \quad (12)$$

$$(q^h, \nabla \cdot \mathbf{u}^h) + (\nabla q^h, \tau_M \mathcal{R}_M^h) = 0 \quad \forall q^h \in \mathcal{V}_p^h. \quad (13)$$

A grad-div term and an SUPG term, first and second term in the second line of (12), and a PSPG term, second term on the left hand side of (13), arise.

The stabilization parameters τ_M and τ_c used in [18] for variable-density flow problems are applied to incompressible two-phase flows:

$$\tau_M = \frac{1}{\sqrt{\left(\frac{2\rho}{\Delta t}\right)^2 + \rho \mathbf{u}^h \cdot \mathbf{G} \rho \mathbf{u}^h + C_1 \mu^2 \mathbf{G} : \mathbf{G}}}, \quad (14)$$

$$\tau_c = \frac{1}{\tau_M \mathbf{g} \cdot \mathbf{g}}, \quad (15)$$

where

$$G_{ij} = \sum_{k=1}^3 \frac{\partial \xi_k}{\partial x_i} \frac{\partial \xi_k}{\partial x_j} \quad \text{and} \quad g_i = \sum_{j=1}^3 \frac{\partial \xi_j}{\partial x_i}$$

utilize the coordinate system ξ of the element domain, see, e.g., [19] for elaboration. The time-step length of the temporal discretization of the problem formulation is denoted by Δt , and C_1 is a positive constant independent of the characteristic element length h . C_1 is chosen to be 36.0 for linearly interpolated finite elements as used in the numerical examples below.

3.2. Level-set formulation

To obtain the variational formulation for the level-set field, an appropriate solution function space \mathcal{S}_{Φ} for Φ and a weighting function space \mathcal{V}_{Φ} for w are assumed: find $\Phi \in \mathcal{S}_{\Phi}$ such that

$$\left(w, \frac{\partial \Phi}{\partial t} \right) + (w, \mathbf{u} \cdot \nabla \Phi) = 0 \quad \forall w \in \mathcal{V}_{\Phi}. \quad (16)$$

Decomposing also the level-set field into resolved and unresolved parts yields

$$\Phi = \Phi^h + \hat{\Phi}, \quad (17)$$

where the subgrid-scale part is given as

$$\hat{\Phi} = -\tau_L \mathcal{R}_L^h. \quad (18)$$

The discrete residual of the level-set equation reads as

$$\mathcal{R}_L^h = \frac{\partial \Phi^h}{\partial t} + \mathbf{u}^h \cdot \nabla \Phi^h.$$

The final residual-based variational multiscale finite element formulation is obtained by introducing decomposition (17) and approximation (18) into the variational formulation (16), integrating by parts the convective term and omitting the subgrid-scale term arising from the transient term as usual: find $\Phi^h \in \mathcal{S}_{\Phi}^h$ such that

$$\begin{aligned} & \left(w^h, \frac{\partial \Phi^h}{\partial t} \right) + (w^h, \mathbf{u}^h \cdot \nabla \Phi^h) + (\mathbf{u}^h \cdot \nabla w^h, \tau_L \mathcal{R}_L^h) = 0, \\ & \forall w^h \in \mathcal{V}_{\Phi}^h. \end{aligned} \quad (19)$$

Analogous to (12), the last term on the left hand side of (19) represents an SUPG term. Adopting (14) for the level-set equation yields

$$\tau_L = \frac{1}{\sqrt{\left(\frac{2}{\Delta t}\right)^2 + \mathbf{u}^h \cdot \mathbf{G} \mathbf{u}^h}}. \quad (20)$$

4. Extension of finite element method

4.1. Representation of discontinuities across interface

When using a fixed-grid scheme, the interface is generally not aligned with the element edges of the mesh. Instead, elements are intersected by the interface. As a consequence of the discontinuities of density and viscosity at the interface, the velocity and the pressure field also involve discontinuities. Because of (3), the velocity field exhibits a kink across the interface, while the pressure field contains a jump across the interface due to (4).

To reproduce discontinuities inside elements, the XFEM is applied. The basic idea of the XFEM is the expansion of standard FEM solution functions via special enriched shape functions. These enriched shape functions with the respective additional degrees of freedom can take into account discontinuities in the solution field. Applied to the velocity field, for example, an enriched approximation can be defined as

$$\mathbf{u}^h(\mathbf{x}, t) = \sum_{A \in \eta} N_A(\mathbf{x}) \mathbf{u}_A(t) + \sum_{\tilde{A} \in \eta_{\text{enr}}} N_{\tilde{A}}(\mathbf{x}) \Psi(\mathbf{x}, t) \tilde{\mathbf{u}}_{\tilde{A}}(t), \quad (21)$$

where the first term is the standard finite element approximation, and the second term is the additional enrichment. Here, η denotes the set of all nodes and η_{enr} the set of enriched nodes, generally a subset of η . The shape function of node A is denoted by N_A , \mathbf{u}_A represents the standard (velocity) degrees of freedom at node A and $\tilde{\mathbf{u}}_{\tilde{A}}$ denotes additional (velocity) degrees of freedom at enriched nodes \tilde{A} . These additional degrees of freedom are multiplied by a properly chosen enrichment function $\Psi(\mathbf{x}, t)$ and $N_A(\mathbf{x})$ to extend the solution. This enrichment strategy is based on a local partition of unity.

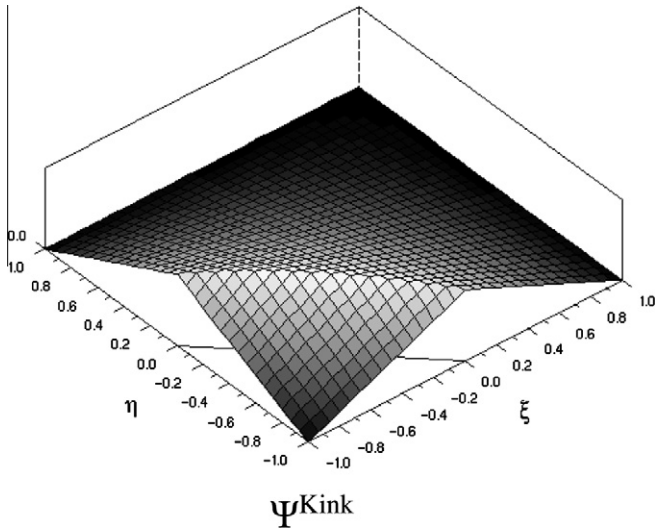


Fig. 2. Kink enrichment function Ψ^{Kink} for a four-noded bilinearly-interpolated quadrilateral element.

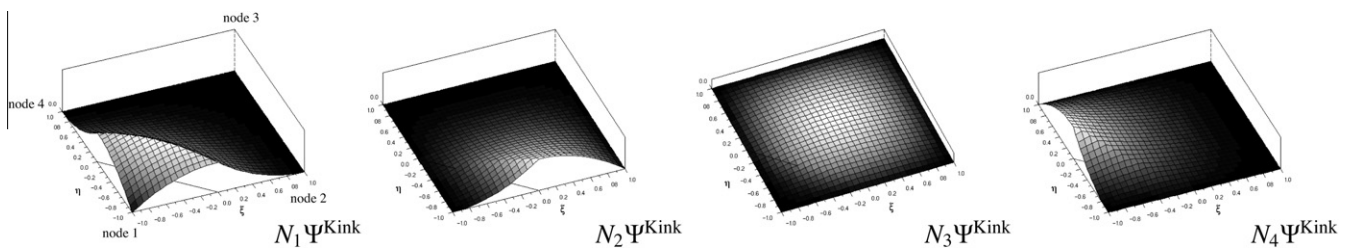


Fig. 3. Kink enrichment: enriched shape functions for a four-noded bilinearly-interpolated quadrilateral element.

The choice of the enrichment function depends on the interface conditions. Following [20], the enrichment function for interface problems involving kinks can be defined as

$$\Psi^{\text{Kink}}(\mathbf{x}, t) = \sum_{A \in \eta} |\Phi_A(t)| N_A(\mathbf{x}) - \left| \sum_{A \in \eta} \Phi_A(t) N_A(\mathbf{x}) \right|, \quad (22)$$

where Φ_A are the nodal values of the level-set field. Fig. 2 depicts the enrichment function for a two-dimensional four-noded bilinearly-interpolated quadrilateral element. The kink is clearly shown. It can be observed that the enrichment function vanishes along edges where non-intersected elements are connected to intersected elements, see also (22). Therefore, the enrichment function is zero in all non-intersected elements. As the enrichment function has zero values at all nodes, it maintains the interpolant property $\mathbf{u}^h(\mathbf{x}_A) = \mathbf{u}_A$. Fig. 3 shows the enriched shape functions of this element.

For modeling jumps, the enrichment function is defined as a (symmetric) Heaviside function

$$\Psi^{\text{Jump}}(\mathbf{x}, t) = \begin{cases} +1 & \Phi(\mathbf{x}, t) \geq 0 \\ -1 & \Phi(\mathbf{x}, t) < 0. \end{cases} \quad (23)$$

To fulfill the interpolant property, a node-dependant enrichment function is constructed by the following modification

$$\Psi_{\tilde{A}}^{\text{Jump}}(\mathbf{x}, t) = \Psi^{\text{Jump}}(\mathbf{x}, t) - \Psi^{\text{Jump}}(\mathbf{x}_{\tilde{A}}, t), \quad (24)$$

where $\Psi_{\tilde{A}}^{\text{Jump}}$ is the final enrichment function and $\mathbf{x}_{\tilde{A}}$ are the coordinates of the enriched node \tilde{A} . Again, the enrichment function vanishes in all non-intersected elements, see Fig. 4.

The complete XFEM solution functions with equal order shape functions N_A for velocity and pressure are given as

$$\mathbf{u}^h(\mathbf{x}, t) = \sum_{A \in \eta} N_A(\mathbf{x}) \mathbf{u}_A(t) + \sum_{\tilde{A} \in \eta_{\text{enr}}} N_{\tilde{A}}(\mathbf{x}) \Psi^{\text{Kink}}(\mathbf{x}, t) \tilde{\mathbf{u}}_{\tilde{A}}(t), \quad (25)$$

$$p^h(\mathbf{x}, t) = \sum_{A \in \eta} N_A(\mathbf{x}) p_A(t) + \sum_{\tilde{A} \in \eta_{\text{enr}}} N_{\tilde{A}}(\mathbf{x}) \Psi^{\text{Kink}}(\mathbf{x}, t) \tilde{p}_{\tilde{A}}(t)$$

$$\text{if } \gamma = 0, \text{ i.e. without surface tension,} \quad (26)$$

$$p^h(\mathbf{x}, t) = \sum_{A \in \eta} N_A(\mathbf{x}) p_A(t) + \sum_{\tilde{A} \in \eta_{\text{enr}}} N_{\tilde{A}}(\mathbf{x}) \Psi_{\tilde{A}}^{\text{Jump}}(\mathbf{x}, t) \tilde{p}_{\tilde{A}}(t)$$

$$\text{if } \gamma > 0, \text{ i.e. with surface tension.} \quad (27)$$

The weighting functions are chosen as usual, that is, the same function spaces are used as for the solution functions.

4.2. Enrichment strategies

Since not all nodes will be enriched, one has to decide which nodes are the enriched ones. First of all, all nodes belonging to an element intersected by the interface are enriched. Therefore, these elements are fully enriched and belong to the subdomain Ω_{enr} . The elements adjacent to the fully enriched elements are called “partially enriched”, as only some of their nodes are enriched. These elements are in the subdomain Ω_{penr} . All remaining

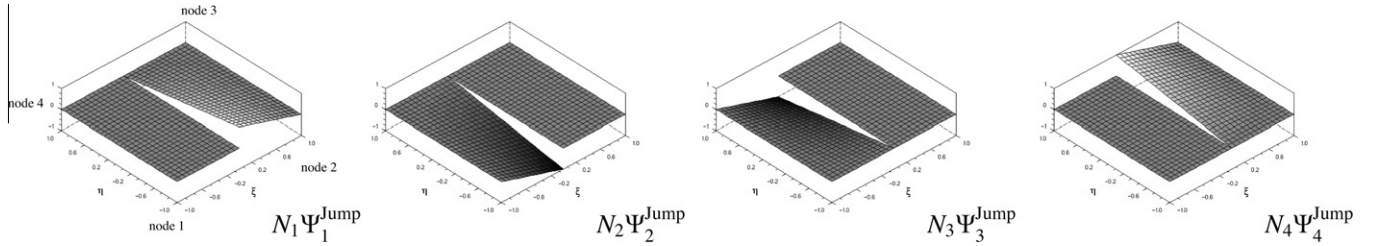


Fig. 4. Jump enrichment: enriched shape functions for a four-noded bilinearly-interpolated quadrilateral element.

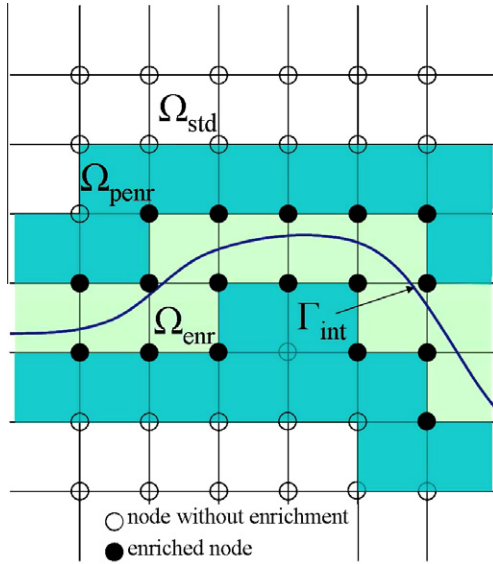


Fig. 5. Subdomains containing enriched, partially enriched and standard (non-enriched) elements as well as the enriched nodes.

elements have only nodes which are not enriched. Consequently, these elements are standard finite elements in the subdomain Ω_{std} . Such a domain decomposition is illustrated in Fig. 5. In contrast to the enrichment functions used in this work, suboptimal convergence rates may occur, if the enrichment function does not vanish in partially enriched elements. To overcome this problem several approaches have been proposed, e.g., in [21].

4.3. Quasi-static enrichment

For temporal discretization, a one-step- θ time-integration scheme is applied to the incompressible Navier–Stokes equations as well as to the level-set equation. In the one-step- θ scheme, the acceleration $\partial \mathbf{u} / \partial t$ is discretized as

$$\frac{\mathbf{u}^{n+1} - \mathbf{u}^n}{\Delta t} = \theta \dot{\mathbf{u}}^{n+1} + (1 - \theta) \dot{\mathbf{u}}^n, \quad (28)$$

where $\dot{\mathbf{u}}$ is defined as

$$\rho \dot{\mathbf{u}} = -\rho \mathbf{u} \cdot \nabla \mathbf{u} - \nabla p + \nabla \cdot (2\mu \varepsilon(\mathbf{u})) + \rho \mathbf{g}.$$

To keep the temporally discretized formulation simple, Eq. (28) is applied to the variational formulation for the fluid field given in (6) and (7):

$$\begin{aligned} & (\mathbf{v}, \rho \mathbf{u}^{n+1}) + \Delta t \theta \left\{ (\mathbf{v}, \rho \mathbf{u}^{n+1} \cdot \nabla \mathbf{u}^{n+1}) - (\nabla \cdot \mathbf{v}, p^{n+1}) \right. \\ & \quad \left. + (\varepsilon(\mathbf{v}), 2\mu \varepsilon(\mathbf{u}^{n+1})) - (\mathbf{v}, \rho \mathbf{g}) - \left(\mathbf{v}, \mathbf{h}_{\mathbf{u}}^{n+1} \right)_{\Gamma_N} - (\mathbf{v}, \gamma \kappa \mathbf{n}_{\text{int}})_{\Gamma_{\text{int}}} \right\} \\ & = (\mathbf{v}, \rho \mathbf{u}^n) + \Delta t (1 - \theta) (\mathbf{v}, \rho \dot{\mathbf{u}}^n), \end{aligned} \quad (29)$$

$$(q, \nabla \cdot \mathbf{u}^{n+1}) = 0. \quad (30)$$

Next, some differences in the time dependencies of the solution and weighting functions of XFEMs compared to standard FEMs have to be pointed out. When employing a semi-discretization approach in the standard FEM, the shape functions are generally constant in time, and only the nodal values are time-dependent. In comparison, additional time dependencies have to be taken into account in XFEMs when moving interfaces are considered. While the standard shape functions are still constant in time, the enriched shape functions are time-dependent, since they depend on the level-set function. Furthermore, the additional enrichment degrees of freedom are time-dependent. Moreover, as only intersected elements are enriched, there are nodes which were enriched at the last time level but are not enriched at the current one and vice versa. That is, new enrichment degrees of freedom are added and some are removed. This has also to be considered in the time-integration in XFEM.

At the beginning of the computation of the fluid field at the current time level, the enriched nodes are identified depending on the intersected elements. The finite element approximation for time level $n + 1$ is then given as

$$\mathbf{u}^{h,n+1}(\mathbf{x}) = \sum_{A \in \eta} N_A(\mathbf{x}) \mathbf{u}_A^{n+1} + \sum_{\tilde{A} \in \eta_{\text{enr}}} N_{\tilde{A}}(\mathbf{x}) \Psi(\mathbf{x}, t^{n+1}) \tilde{\mathbf{u}}_{\tilde{A}}^{n+1}. \quad (31)$$

In contrast, to construct the enrichment function at time level n , the corresponding interface position is required. An approximation of the solution field at the previous time level only by the standard finite element part avoids retaining the necessary information at time level n . Neglecting the enrichment of the previous time level, the following approximation is obtained:

$$\mathbf{u}^{h,n}(\mathbf{x}) = \sum_{A \in \eta} N_A(\mathbf{x}) \mathbf{u}_A^n. \quad (32)$$

Due to the time dependence of the enriched shape functions, not only the solution functions but also the weighting functions are time-dependent. In accordance to the aforementioned solution function, the weighting function is chosen corresponding to the current time level $n + 1$:

$$\mathbf{v}^h = \mathbf{v}^{h,n+1}.$$

The same approach is applied to the solution and weighting functions of the pressure. In summary, this yields a quasi-static enrichment.

In this context, the reader is also referred to, e.g., [22] for the discussion therein on using space-time XFEMs as an alternative. For computing dynamic problems with XFEM in fracture mechanics, the reader is referred to, e.g., [23].

4.4. Numerical integration

If an element is intersected by the interface, it is important to clearly distinguish the respective sides of the interface to appropriately set the correct viscosities and densities. Moreover, simple quadrature rules such as Gaussian quadrature are developed to

integrate polynomials and, hence, do not work well for discontinuous functions such as the enriched shape functions. To avoid having to numerically integrate discontinuous functions, intersected elements are sub-divided into element subdomains which are either in the domain Ω^+ or Ω^- , see, e.g., [6]. Here, the sub-division is done in two steps. In the first optional step, intersected elements are split up into element subdomains of the same shape as the element in consecutive refinement steps. Then, intersected element subdomains are further sub-divided with respect to the interface using a constrained Delaunay triangulation (or tetrahedralization) as described in, e.g., [24] and used in, e.g., [25]. The algorithm used to construct the subdomains simultaneously builds a set of surface patches, which approximately form the interface and can be used to reinitialize the level-set as well as to evaluate interface integrals resulting from a non-zero surface tension. Similar algorithms can be found, for example, in [5] and [26].

5. Numerical examples

In this section, simulation results of two- and three-dimensional two-phase flow problems are shown. The following statements apply to all numerical examples below.

- Trilinearly-interpolated hexahedral elements are used for the fluid and the level-set field.
- In the two-dimensional case, flows are computed with only one element layer in the third dimension. Slip boundary conditions for the fluid field are applied at the surfaces orthogonal to the respective two-dimensional computational domain.
- As the level-set values are used to construct the kink enrichment function and the velocity of the fluid field convects the interface, these two solution fields have to be transferred between fluid and level-set solver. By employing the same spatial discretization (i.e., mesh and element type) for fluid and level-set field, velocity values and level-set values can be easily transferred, and projections of the velocity space to the level-set space and vice versa are not necessary.
- For both flow and level-set field, the parameter θ of the time-integration scheme is chosen to be $\theta = 0.5$ for all instationary examples, that is, a Crank–Nicolson scheme is used. Exceptions are indicated below.
- The approximation of the localized surface tension force is based on a Laplace–Beltrami approximation. Using the Laplace–Beltrami operator and integrating by parts, the surface tension term is reformulated as

$$(\mathbf{v}, \gamma \kappa \mathbf{n}_{\text{int}})_{\Gamma_{\text{int}}} = -(\mathbf{v}, \gamma \Delta_{\Gamma_{\text{int}}} \mathbf{id})_{\Gamma_{\text{int}}} = (\nabla_{\Gamma_{\text{int}}} \mathbf{v}, \gamma \nabla_{\Gamma_{\text{int}}} \mathbf{id})_{\Gamma_{\text{int}}},$$

where the Laplace–Beltrami operator is defined as $\Delta_{\Gamma_{\text{int}}} f = \nabla_{\Gamma_{\text{int}}} \cdot \nabla_{\Gamma_{\text{int}}} f$ with the tangential derivative along Γ_{int} $\nabla_{\Gamma_{\text{int}}} f = \nabla f - \nabla f \cdot \mathbf{n}_{\text{int}} \mathbf{n}_{\text{int}}$ and \mathbf{id} is an identity mapping on the interface. A potential boundary term due to interfaces that are not closed is omitted here for the sake of brevity. To improve the approximation quality of the discretized surface tension force, a modified surface tension force discretization as proposed in [27] and applied in combination with XFEM to stationary bubbles with pressure jump in [8] is used. The discretized interface Γ_{int}^h consists of planar surface patches as described in Section 4.4. The normal vector $\mathbf{n}_{\text{int}}^h$ on Γ_{int}^h is piecewise constant. Defining the orthogonal projection $\mathbf{P}^h = \mathbf{I} - \mathbf{n}_{\text{int}}^h (\mathbf{n}_{\text{int}}^h)^T$, we have $\nabla_{\Gamma_{\text{int}}^h} f = \mathbf{P}^h \nabla f$. Instead of using the piecewise constant normal vector $\mathbf{n}_{\text{int}}^h$, it is proposed to compute a smoother normal vector $\bar{\mathbf{n}}_{\text{int}}^h$ by the use of the level-set function in [27]

$$\bar{\mathbf{n}}_{\text{int}}^h = \frac{\nabla \phi^h}{\|\nabla \phi^h\|}.$$

As trilinearly-interpolated hexahedral elements are used for the level-set field, the gradient of the level-set field cannot be computed with the required accuracy. To overcome this difficulty, a least squares procedure as used, e.g., in [30] to compute nodal gradients of the level-set field is applied. Altogether, the final discrete surface tension term is given as

$$(\nabla_{\Gamma_{\text{int}}^h} \mathbf{v}^h, \gamma \nabla_{\Gamma_{\text{int}}^h} \mathbf{id})_{\Gamma_{\text{int}}^h} = (\nabla_{\Gamma_{\text{int}}^h} \mathbf{v}^h, \gamma \bar{\mathbf{P}}^h)_{\Gamma_{\text{int}}^h},$$

where $\bar{\mathbf{P}}^h = \mathbf{I} - \bar{\mathbf{n}}_{\text{int}}^h (\bar{\mathbf{n}}_{\text{int}}^h)^T$.

- It is accounted for the non-linearity of the system of equations by using a Picard (or fixed-point-like) iteration scheme based on an incremental formulation of the resulting matrix system. Usually, five iterations were sufficient to reach a prescribed tolerance of 10^{-5} . For solving the final linear equation system, an AMG-preconditioned GMRES solver is applied. As demonstrated, for example, in [28], large flow problems can be solved efficiently by this approach.

5.1. Couette two-phase flow

In the first example, the basic ability of the method to accurately simulate two-phase flows with an interface not conforming to the mesh is investigated for the case of a two-dimensional fully developed Couette flow. The considered domain is $\Omega = [-L, L] \times [-H, H]$ with $L = 4$ m and $H = 1$ m. Two immiscible fluids are separated by an interface located at $x_2 = 0$ m. This simple stationary test case does not include any deformation of the interface. The upper subdomain is denoted by Ω^+ , the lower by Ω^- . Both fluids have the same density $\rho^+ = \rho^- = 1.0$ kg/m³. The dynamic viscosity of the fluid in domain Ω^+ is $\mu^+ = 0.1$ kg/(ms), and the viscosity of the fluid in domain Ω^- is $\mu^- = 0.02$ kg/(ms). Gravitation is not considered in this example.

No-slip boundary conditions are prescribed at both walls of the channel. While the lower wall is at rest, the upper wall is moving in x_1 -direction with constant velocity $U_0 = 5$ m/s. At the inlet and the outlet of the channel, the x_2 -component of the velocity is set to zero. A spatial discretization of 20×5 finite elements is used, so that one row of elements is intersected in the middle by the interface. The purpose of this example is to illustrate the effect of the enrichment in correctly capturing the discontinuity in the velocity gradient. The exact solution assuming fully developed flow is

$$u_1 = \begin{cases} \frac{U_0 \mu^-}{\mu^+ + \mu^-} \frac{x_2}{H} + \frac{U_0 \mu^+}{\mu^+ + \mu^-} & 0 \leq x_2 \leq H, \\ \frac{U_0 \mu^+}{\mu^+ + \mu^-} \frac{x_2}{H} + \frac{U_0 \mu^-}{\mu^+ + \mu^-} & -H \leq x_2 < 0, \end{cases}$$

$$u_2 = 0,$$

$$p = p_0.$$

The resulting velocity field is depicted in Fig. 6. The discontinuity in the velocity gradient along the interface can be clearly observed. As expected for this example, the analytical solution is obtained exactly.

5.2. Rayleigh–Taylor instability

In the next example, a two-dimensional Rayleigh–Taylor instability is examined. This flow example was also considered, e.g., in [5]. A heavy fluid is located above a light fluid in a rectangular domain $\Omega = [-L, L] \times [-H, H]$ with $L = 0.5$ m and $H = 2.0$ m. The interface between the fluids has initially a cosine shape with amplitude 0.05 m subject to

$$x_2 = 0.05 \cos(2\pi x_1).$$

In the first Rayleigh–Taylor instability, the densities of the fluids are $\rho^+ = 3.0$ kg/m³ and $\rho^- = 1.0$ kg/m³, and the dynamic viscosities

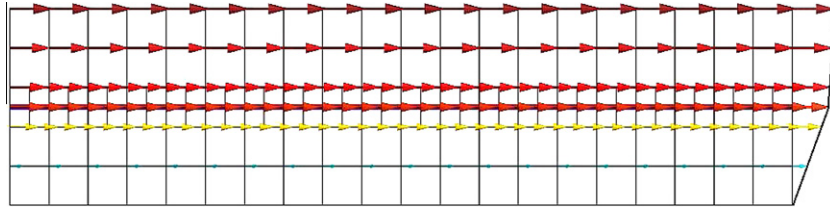


Fig. 6. Couette flow: velocity vectors colored by velocity magnitude, interface (bold line) and element subdomains indicating the enriched elements (red color indicates high velocity, blue color indicates low velocity, post-processed using Gmsh [29]). (For interpretation of the references to color in this figure legend, the reader is referred to the web version of this article.)

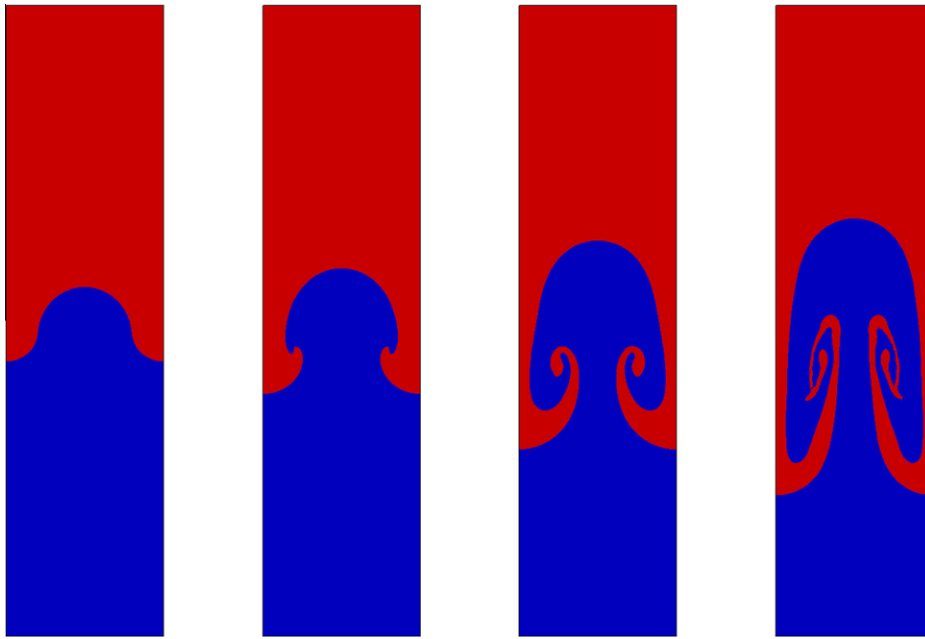


Fig. 7. Evolution of Rayleigh–Taylor instability ($Re = 500$, $A = 0.5$) at times $t = 0.50, 0.70, 1.00, 1.25$ s.

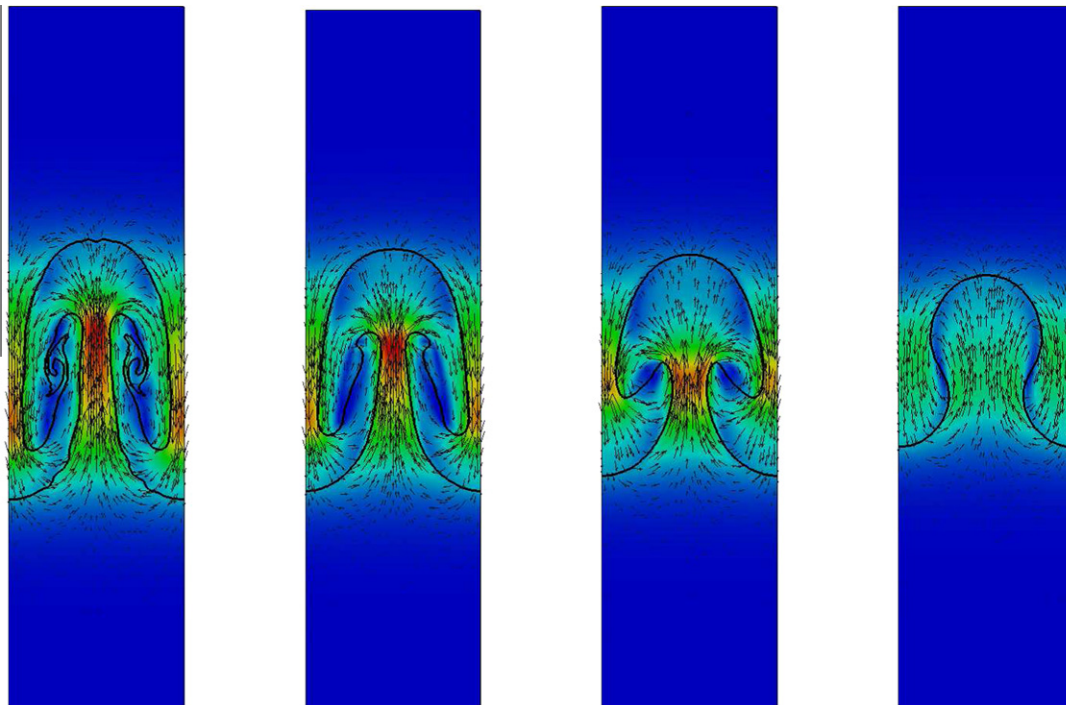


Fig. 8. Rayleigh–Taylor instability ($Re = 1000$, $A = 0.2$) at time $t = 1.85$ s for $\gamma = 0.00, 0.03, 0.06, 0.09$ kg/s²: interface position and velocity vectors on colored velocity magnitude distribution (red color indicates high velocity, blue color indicates low velocity). (For interpretation of the references to color in this figure legend, the reader is referred to the web version of this article.)

are $\mu^+ = 0.0135 \text{ kg/(ms)}$ and $\mu^- = 0.0045 \text{ kg/(ms)}$. The gravitation vector is $\mathbf{g} = (0, -10.0 \text{ m/s}^2)^T$, resulting in the same dimensionless numbers as in [5]. The Reynolds number is $\text{Re} = \sqrt{gHL\rho^-}/\mu^- = \sqrt{gHL\rho^+}/\mu^+ = 500$. The Atwood number for this case is $A = \frac{\rho^+ - \rho^-}{\rho^+ + \rho^-} = 0.5$.

Initially, a zero velocity field is assumed. Slip boundary conditions are prescribed at all boundaries of the domain. The mesh consists of 64×256 elements. A time-step length of $\Delta t = 0.01 \text{ s}$ is used. The simulations are advanced until the finest structures are of the order of the element size. Fig. 7 shows the evolution of the interface at different times. As expected, the heavy fluid falls into the light one and rolls up in two counter rotating vortices. A confirmation of the present results may be obtained by comparing them with the results given in [5], Fig. 17. The maximum mass fluctuation is approximately 0.10%. In [5], a mass fluctuation of 0.07% was observed for a second-order level-set scheme.

To demonstrate the ability of the approach for accurately simulating flows with higher Reynolds number, a second Rayleigh–Taylor instability is examined. Here, the densities of the fluids are $\rho^+ = 1.5 \text{ kg/m}^3$ and $\rho^- = 1.0 \text{ kg/m}^3$, and the dynamic viscosities are $\mu^+ = 0.0033 \text{ kg/(ms)}$ and $\mu^- = 0.0022 \text{ kg/(ms)}$. Again, the gravitation vector is $\mathbf{g} = (0, -10.0 \text{ m/s}^2)^T$. The resulting dimensionless numbers are $\text{Re} = 1000$ and $A = 0.2$. In addition, various surface tension coefficients are examined. The simulations are performed for $\gamma = 0.00, 0.03, 0.06$ and 0.09 kg/s^2 . The same initial and boundary conditions are prescribed, and the same discretization as in the preceding example is used. A time-step length of $\Delta t = 0.01 \text{ s}$ is used for $\gamma = 0.00$ and 0.03 kg/s^2 , whereas $\Delta t = 0.005 \text{ s}$

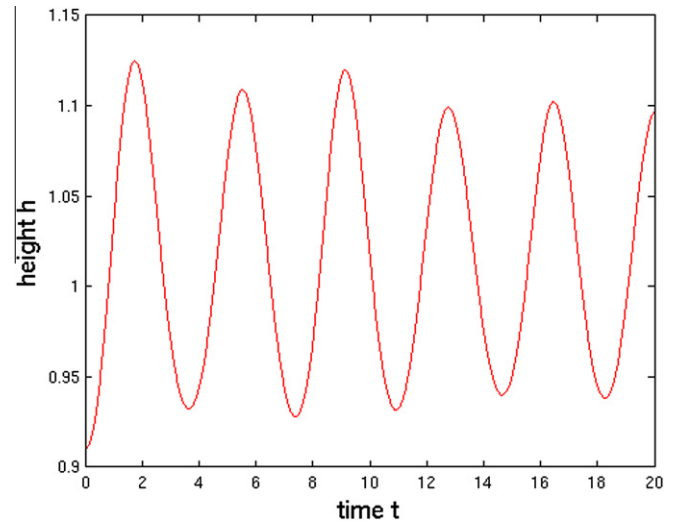


Fig. 10. Interface position h at left wall of the tank.

is chosen for $\gamma = 0.06$ and 0.09 kg/s^2 owing to the higher surface tension. The parameter θ of the time-integration scheme is chosen to be $\theta = 0.65$ for more robustly solving the flow field, since a Crank–Nicolson time-integration scheme turned out not to fully guarantee a stable solution for this second Rayleigh–Taylor instability. Fig. 8 depicts the interface at time $t = 1.85 \text{ s}$ along with the corresponding

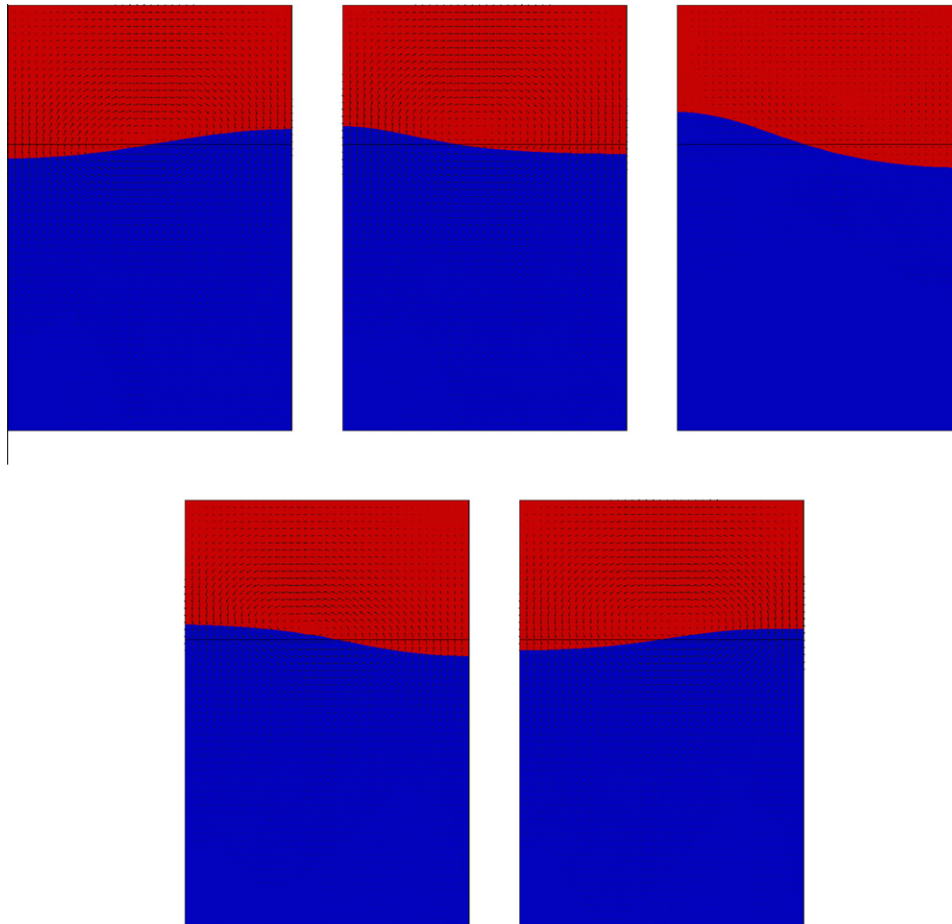


Fig. 9. Sloshing tank: position of the interface and velocity vectors at times $t = 0.6, 1.2, 1.8, 2.4, 3.0 \text{ s}$.

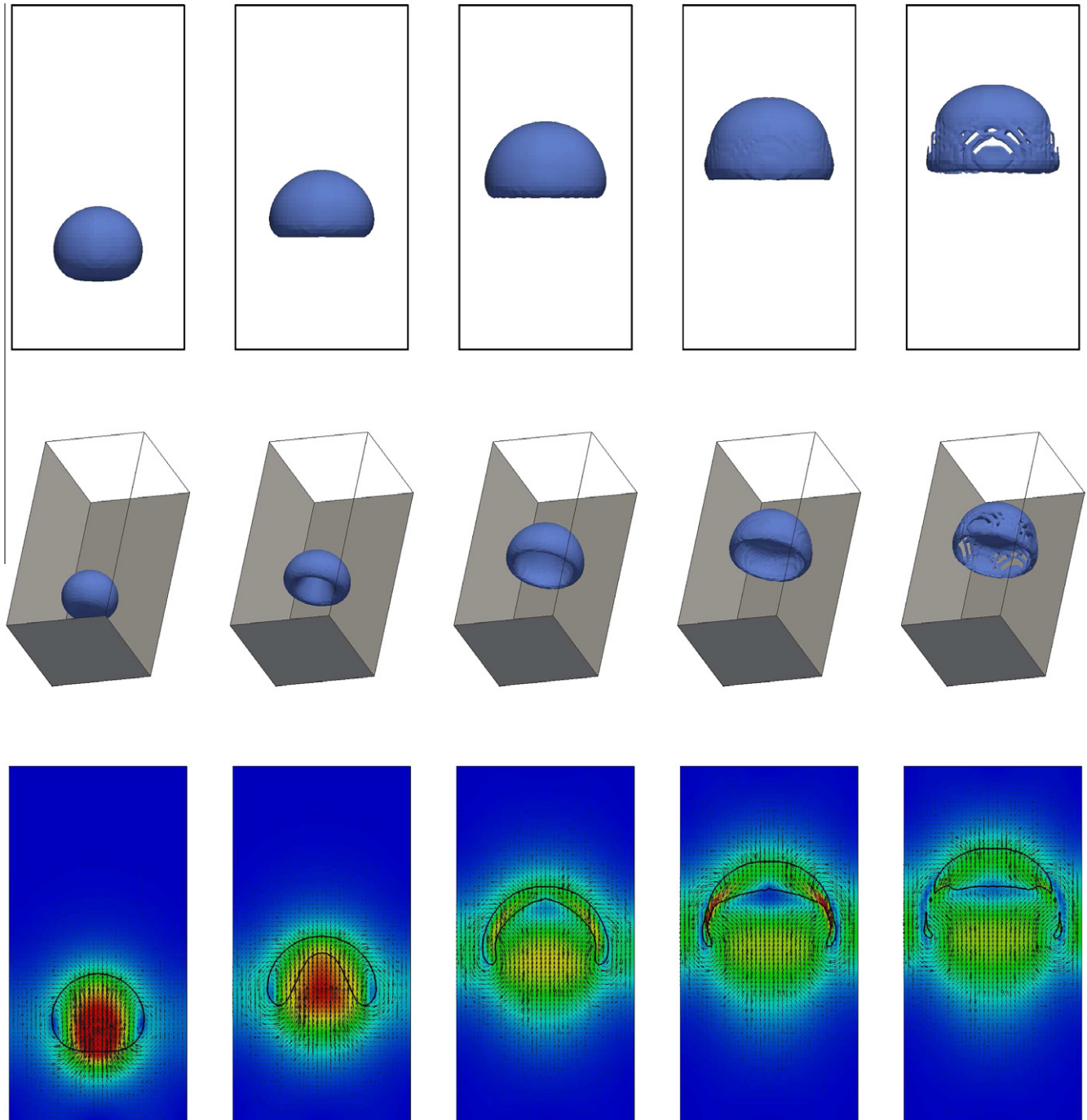


Fig. 11. Rising bubble ($\gamma = 0.0$) at times $t = 0.04, 0.1, 0.18, 0.22, 0.24$ s: three-dimensional shape of the bubble as well as interface and velocity vectors on colored velocity magnitude distribution in x_1x_3 -plane (red color indicates high velocity, blue color indicates low velocity). (For interpretation of the references to color in this figure legend, the reader is referred to the web version of this article.)

velocity vectors for $\gamma = 0.00, 0.03, 0.06$ and 0.09 kg/s^2 . It can be observed that surface tension prevents the interface to roll up.

5.3. Sloshing tank

Two-phase flow in a two-dimensional sloshing tank is considered in this example. This flow example was also investigated, e.g., in [14]. Following [14], the problem domain is $\Omega = [-L, L] \times [-H, H]$, where $L = 0.5 \text{ m}$ and $H = 0.75 \text{ m}$. The interface separating the two phases is initially given as

$$x_2 = 0.26 + 0.1 \sin(\pi x_1).$$

The densities of the fluids are $\rho^+ = 1.0 \text{ kg/m}^3$ and $\rho^- = 1000.0 \text{ kg/m}^3$, and the dynamic viscosities are $\mu^+ = 0.01 \text{ kg/(ms)}$ and $\mu^- = 1.00 \text{ kg/(ms)}$. A gravitation vector $\mathbf{g} = (0, -1.0 \text{ m/s}^2)^T$ is considered. Slip-boundary conditions are prescribed along the walls of the tank, and a zero velocity field is initially assumed. The domain is discretized with 40×60 elements. The time-step length is $\Delta t = 0.015 \text{ s}$, and the simulation is advanced until $t_{\text{end}} = 20.0 \text{ s}$. A Crank–Nicolson time-integration scheme for solving the flow field turned out not to fully guarantee a stable solution. Hence, a value of $\theta = 0.65$ is chosen for more robustly solving the flow field in this particular example. As will be shown in the qualitative and quantitative evaluation below, this slight reduction in the order of accuracy of the

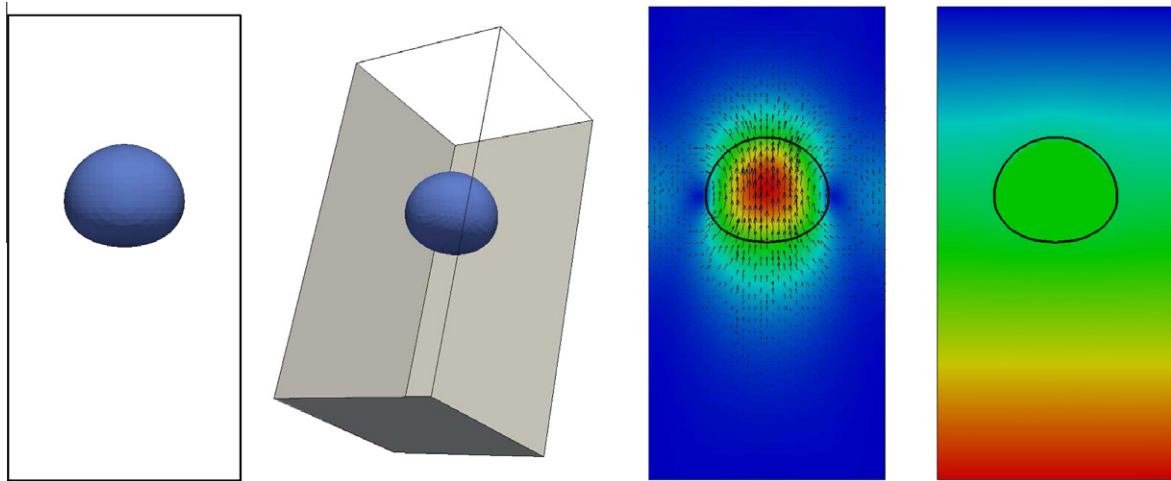


Fig. 12. Rising bubble ($\gamma = 0.11$) at time $t = 0.15$ s: three-dimensional shape of the bubble, interface and velocity vectors on colored velocity magnitude distribution as well as interface and pressure distribution in x_1x_3 -plane (red color indicates high velocity/pressure, blue color indicates low velocity/pressure). (For interpretation of the references to color in this figure legend, the reader is referred to the web version of this article.)

time-integration scheme with respect to the flow field does not degrade the overall solution.

Fig. 9 shows the evolution of the interface at selected points in time. For confirmation, these patterns may be compared to the respective patterns displayed in Fig. 15(b) in [14]. The position h where the interface cuts the left boundary is depicted over time in Fig. 10. The frequency of the oscillation is 0.274 Hz, which well agrees with 0.279 Hz, the value reported in [14].

5.4. Rising bubble

The rise and deformation of a three-dimensional gas bubble in liquid contained in a vertical, rectangular container is investigated. Three-dimensional rising bubbles were examined using standard FEMs in, e.g., [4,30]. For the simulation of a single bubble, the computational domain is $\Omega = [-D, D] \times [-D, D] \times [-2D, 2D]$, depending on the diameter D of the bubble. Initially, the bubble is at rest, and the center of the bubble is located at $x_3 = -D$. A zero velocity field is prescribed. Following [4], the density and the viscosity of the outer fluid are $\rho^+ = 1000.0 \text{ kg/m}^3$ and $\mu^+ = 0.35 \text{ kg/(ms)}$. For the bubble, density $\rho^- = 1.225 \text{ kg/m}^3$ and viscosity $\mu^- = 0.00358 \text{ kg/(ms)}$ are prescribed. Hence, the density ratio is approximately 816, and the viscosity ratio approximately 100. The gravitation vector is $\mathbf{g} = (0, 0, -9.81 \text{ m/s}^2)^T$.

Two bubbles are investigated. The initial diameter of the first bubble without effect of surface tension (i.e. $\gamma = 0.0 \text{ kg/s}^2$) is $D = 0.05 \text{ m}$, and therefore, $\text{Re} = \frac{\sqrt{DgD\rho^+}}{\mu^+} = 100$. For the second simulation a surface tension coefficient of $\gamma = 0.11 \text{ kg/s}^2$ is applied. The initial diameter of this bubble is $D = 0.01 \text{ m}$, resulting in the following dimensionless numbers: the Morton number is $\text{Mo} = \frac{g(\mu^+)^4}{\rho^+\gamma^3} = 0.1$, the Eötvös number is $\text{Eo} = \frac{(\rho^+ - \rho^-)gD^2}{\gamma} = 10$ and the Reynolds number is $\text{Re} = 10$. The bubble is advanced until it is affected by the top of the container. Slip boundary conditions are assumed at all boundaries of the domain. The domain is discretized with $40 \times 40 \times 80$ elements.

Fig. 11 depicts the evolution of the first bubble at various times as well as the velocity vectors in the x_2x_3 -plane ($x_1 = 0$) along with the interface. The time-step length is chosen to be $\Delta t = 0.002 \text{ s}$ for this example. Due to the buoyancy force, the bubble begins to rise, and a velocity field emerges which induces a jet of water that pushes into the bubble from below. At this stage, the velocity of the upper surface in comparison to the velocity of the lower surface is low. For low surface tension or neglected surface tension,

the jet of water is able to move the lower surface of the bubble upward and, hence, deforms the bubble. As a result, the bubble takes the form of a cap. While the lower surface moves toward the upper surface, the cap gets thinner with increasing radii. Finally, a skirted bubble is formed. The trailing edge of the skirted bubble then breaks off in a series of small bubbles and the remaining bubble takes the form of a spherical cap. The shapes of the bubble are similar to, e.g., the results from the respective two-dimensional simulation including low surface tension in [4] (see Figs. 4–6 therein).

In the second case, a time-step length of $\Delta t = 0.0015 \text{ s}$ is used. The bubble is only slightly deformed to an ellipsoidal shape due to surface tension. Then, it rises with constant velocity. The final shape, the velocity vectors as well as the pressure field in the x_2x_3 -plane ($x_1 = 0$) along with the interface are shown in Fig. 12. The jump in the pressure field can be clearly observed. It can be seen that the shape of the bubble is in agreement with the form predicted by the bubble diagram of Grace and co-workers [31], which is based on experimental data. Moreover, the results conform with the respective simulations reported in [30] (see Fig. 12(b) and 13 therein).

6. Conclusions

An extended residual-based variational multiscale method has been proposed for two-phase flows. In this approach, we have combined residual-based variational multiscale formulations for both fluid and level-set equation with the extended finite element method. In the context of the extended finite element method, a quasi-static enrichment strategy has been proposed to capture time-dependent discontinuities in the solution field. The level-set method has been employed to represent the interface on a fixed mesh. An extended finite element method similar to the approaches proposed in, e.g., [7,8,13] has been applied. In contrast, an intrinsic extended finite element method without additional enrichment degrees of freedom was shown in [14], enrichments based on bubble functions were presented in [15], and a method containing element enrichments for the pressure was proposed in [16]. Kink enrichment for the velocity was examined in [7]. In that work, the convective terms were stabilized by a characteristic based split method. In [8,13], problems governed by the Stokes equations were investigated using inf-sup-stable elements. Jumps in the pressure field were examined in [8], and kink enrichment functions for n -phase flows were developed in [13]. Compared to

those aforementioned extended finite element methods for two-phase flow, we have proposed an extended finite element method with kink enrichments of both velocity and pressure as well as kink enrichments of velocity and jumps enrichments of pressure combined with residual-based variational multiscale formulations for both fluid and level-set equation.

Four numerical test cases of increasing complexity have been considered in this study: a two-dimensional two-phase Couette flow, a two-dimensional Rayleigh–Taylor instability, a two-dimensional sloshing tank and a three-dimensional rising bubble. The first example, which represents a stationary problem with non-deforming interface, has been chosen to demonstrate the ability of the method to accurately resolve discontinuities inside elements. Next, Rayleigh–Taylor instabilities have been examined for two different Reynolds numbers and different surface tension coefficients. Also in the third example, a sloshing tank, accurate results have been obtained. Finally, three-dimensional rising bubbles with and without surface tension have been investigated to demonstrate the presented method for a substantially more complex example; to the best of the authors' knowledge, there have not yet been published results for such an instationary problem configuration using an XFEM. Hence, in summary, the ability of the approach to compute two- and three-dimensional instationary two-phase flows from small to very large density and viscosity ratios has been shown. Stable and accurate results have been obtained for all examples.

Acknowledgments

Support via the Emmy Noether Program of the Deutsche Forschungsgemeinschaft (DFG) is gratefully acknowledged. Furthermore, the authors would like to thank Benedikt Schott for his contribution to the present study.

References

- [1] S. Osher, R. Fedkiw, *Level Set Methods and Dynamic Implicit Surfaces*, Springer-Verlag, New York, 2003.
- [2] J.A. Sethian, P. Smereka, Level set methods for fluid interfaces, *Ann. Rev. Fluid Mech.* 35 (2003) 341–372.
- [3] M. Sussman, P. Smereka, S. Osher, A level set approach for computing solutions to incompressible two-phase flow, *J. Comput. Phys.* 114 (1994) 146–159.
- [4] S. Nagrath, K.E. Jansen, R.T. Lahey Jr., Computation of incompressible bubble dynamics with a stabilized finite element level set method, *Comput. Methods Appl. Mech. Engrg.* 194 (2005) 4565–4587.
- [5] E. Marchandise, J.-F. Remacle, A stabilized finite element method using a discontinuous level set approach for solving two phase incompressible flows, *J. Comput. Phys.* 219 (2006) 780–800.
- [6] N. Moës, J. Dolbow, T. Belytschko, A finite element method for crack growth without remeshing, *Int. J. Numer. Methods Engrg.* 46 (1999) 131–150.
- [7] J. Chessa, T. Belytschko, An extended finite element method for two-phase fluids, *J. Appl. Mech.* 70 (2003) 10–17.
- [8] S. Groß, A. Reusken, An extended pressure finite element space for two-phase incompressible flows with surface tension, *J. Comput. Phys.* 224 (2007) 40–58.
- [9] T.J.R. Hughes, G.R. Feijoo, L. Mazzei, J.-B. Quincy, The variational multiscale method—a paradigm for computational mechanics, *Comput. Methods Appl. Mech. Engrg.* 166 (1998) 3–24.
- [10] M. Braack, E. Burman, V. John, G. Lube, Stabilized finite element methods for the generalized Oseen problem, *Comput. Methods Appl. Mech. Engrg.* 196 (2007) 853–866.
- [11] Y. Bazilevs, V.M. Calo, J.A. Cottrell, T.J.R. Hughes, A. Reali, G. Scovazzi, Variational multiscale residual-based turbulence modeling for large eddy simulation of incompressible flows, *Comput. Methods Appl. Mech. Engrg.* 197 (2007) 173–201.
- [12] O.C. Zienkiewicz, R. Codina, A general algorithm for compressible and incompressible flow, Part I, The split characteristic based scheme, *Int. J. Numer. Methods Fluids* 20 (1995) 869–885.
- [13] S. Zlotnik, P. Diez, Hierarchical XFEM for n-phase flow ($n > 2$), *Comput. Methods Appl. Mech. Engrg.* 198 (2009) 2329–2338.
- [14] T.P. Fries, The intrinsic XFEM for two-phase flows, *Int. J. Numer. Methods Fluids* 60 (2009) 437–471.
- [15] P.D. Mineev, T. Chen, K. Nandakumar, A finite element technique for multifluid incompressible flow using Eulerian grids, *J. Comput. Phys.* 187 (2003) 255–273.
- [16] A.H. Coppola-Owen, R. Codina, Improving Eulerian two-phase flow finite element approximation with discontinuous gradient pressure shape functions, *Int. J. Numer. Methods Fluids* 49 (2005) 1287–1304.
- [17] F. Losasso, R. Fedkiw, S. Osher, Spatially adaptive techniques for level set methods and incompressible flow, *Comput. Fluids* 35 (2006) 995–1010.
- [18] V. Gravemeier, W.A. Wall, Residual-based variational multiscale methods for laminar, transitional and turbulent variable-density flow at low Mach number, *Int. J. Numer. Meth. Fluids*, in press, available online: <<http://dx.doi.org/10.1002/flid.2242>>.
- [19] T.J.R. Hughes, *The Finite Element Method: Linear Static and Dynamic Finite Element Analysis*, Prentice-Hall, Englewood Cliffs, NJ, 1987.
- [20] N. Moës, M. Cloirec, P. Cartraud, J.-F. Remacle, A computational approach to handle complex microstructure geometries, *Comput. Methods Appl. Mech. Engrg.* 192 (2003) 3163–3177.
- [21] J. Chessa, H. Wang, T. Belytschko, On the construction of blending elements for local partition of unity enriched finite elements, *Int. J. Numer. Methods Engrg.* 57 (2003) 1015–1038.
- [22] J. Chessa, T. Belytschko, Arbitrary discontinuities in space-time finite elements by level sets and XFEM, *Int. J. Numer. Methods Engrg.* 61 (2004) 2595–2614.
- [23] J. Réthoré, A. Gravouil, A. Combescure, An energy-conserving scheme for dynamic crack growth using the extended finite element method, *Int. J. Numer. Methods Engrg.* 63 (2005) 631–659.
- [24] U.M. Mayer, A. Gerstenberger, W.A. Wall, Interface handling for three-dimensional higher-order XFEM-computations in fluid-structure interaction, *Int. J. Numer. Methods Engrg.* 47 (2009) 846–869.
- [25] A. Gerstenberger, W.A. Wall, An extended finite element method/Lagrange multiplier based approach for fluid-structure interaction, *Comput. Methods Appl. Mech. Engrg.* 197 (2007) 1699–1714.
- [26] F. van der Bos, V. Gravemeier, Numerical simulation of premixed combustion using an enriched finite element method, *J. Comput. Phys.* 228 (2009) 3605–3624.
- [27] S. Groß, A. Reusken, Finite element discretization error analysis of a surface tension force in two-phase incompressible flows, Preprint 262, IGPM, RWTH Aachen, SIAM J. Numer. Anal. 45 (2007) 1679–1700.
- [28] V. Gravemeier, W.A. Wall, An algebraic variational multiscalemultigrid method for large-eddy simulation of turbulent variable-density flow at low Mach number, *J. Comput. Phys.* 229 (2010) 6047–6070.
- [29] C. Geuzaine, J.-F. Remacle, Gmsh: a three-dimensional finite element mesh generator with built-in pre- and post-processing facilities, *Int. J. Numer. Methods Engrg.* 79 (2009) 1309–1331.
- [30] E. Marchandise, P. Geuzaine, N. Chevaugeon, J.-F. Remacle, A stabilized finite element method using discontinuous level set approach for the computation of bubble dynamics, *J. Comput. Phys.* 225 (2007) 949–974.
- [31] R. Clift, J. Grace, M. Weber, *Bubbles, Drops and Particles*, Academic Press, New York, 1978.